Surface & Coatings Technology 518 (2025) 132879

Contents lists available at ScienceDirect

Surface & Coatings Technology

journal homepage: www.elsevier.com/locate/surfcoat

Out-of-sync co-evaporation in atom probe tomography: Shifting perspectives on compositional biases in TiC and TiN coatings

Maximilian Schiester [a,*], Marcus Hans [b], Daniel Primetzhofer [c], Jan Köttgen [d], Christoph Czettl [e], Nina Schalk [f], Michael Tkadletz [a]

[a] Christian Doppler Laboratory for Sustainable Hard Coatings at the Department of Materials Science, Montanuniversität Leoben, Franz-Josef-Straße 18, 8700 Leoben, Austria
[b] Materials Chemistry, RWTH Aachen University, Kopernikusstraße 10, 52074 Aachen, Germany
[c] Department of Physics and Astronomy, Uppsala University, Lägerhyddsvägen 1, 75120 Uppsala, Sweden
[d] Institute of Physics (IA), RWTH Aachen University, Sommerfeldstraße 14, 52074 Aachen, Germany
[e] CERATIZIT Austria GmbH, Metallwerk-Plansee-Straße 71, 6600 Reutte, Austria
[f] Department of Materials Science, Montanuniversität Leoben, Franz-Josef-Straße 18, 8700 Leoben, Austria

ARTICLE INFO

Keywords:
APT
Elemental accuracy
Background analysis
Multiple detection events
Correlative evaporation
Evaporation behavior
Molecular ions

ABSTRACT

Atom probe tomography (APT) offers unparalleled three-dimensional insights into the nanoscale composition of advanced materials. However, the presence of multiple detection events, charge state distributions as well as molecular ions and consequent compositional biases complicate quantitative analyses. In this study, the phenomenon of out-of-sync co-evaporation in binary transition metal carbides and nitrides is explored through a comparative study of TiC and TiN coatings. These coatings, synthesized by chemical vapor deposition on cemented carbide substrates, were investigated using a reflectron-based LEAP 5000 XR and a straight-flight-path LEAP 5000 XS atom probe in laser-assisted mode. For validation, time-of-flight elastic recoil detection analysis, Rutherford backscattering spectrometry and elastic backscattering spectrometry were employed to obtain accurate reference compositions.

Ion correlation histograms and out-of-sync co-evaporation plots were used to analyze compositional biases and field evaporation behavior. TiC exhibited pronounced thermal tails in the mass spectrum and structured ion patterns in the ion correlation histogram. Co-evaporation plots revealed tracks for both synchronous and out-of-sync evaporation, predominantly involving C-containing ion pairs. In contrast, TiN showed minor thermal tails, but a variety of vertical tracks, indicating out-of-sync co-evaporation. Additionally, its stronger tendency for molecular ion formation further complicates the evaporation analysis.

This work unveils the complex interplay of field evaporation mechanisms in transition metal carbides and nitrides, while introducing an analysis tool for more accurate characterization of compound materials. By utilizing the commonly neglected background, crucial insights into APT analyses are gained and thus, could play a pivotal role in paving the way toward increased measurement accuracy.

1. Introduction

Atom probe tomography (APT) enables high-resolution compositional analysis by providing three-dimensional nanoscale insights into materials by combining position-sensitive detection of ions with time-of-flight (ToF) mass spectrometry [1]. While this technique has significantly advanced the understanding of materials at the near-atomic scale, challenges remain regarding the accurate quantification of the elemental composition. In particular, compositional biases have been reported in a wide range of material systems, particularly for oxides, nitrides, carbides, and borides [2–11]. Despite extensive research, the exact mechanisms leading to these biases are still not fully understood, and further investigation is required to clarify how field evaporation conditions affect the measured compositions.

Chemically simple TiC and TiN coatings have been widely used as wear-resistant coatings on cutting tools for decades and paved the way for state-of-the-art protective coating systems such as TiCN or TiAlN [12–14]. However, their analysis in APT is complicated due to the

* Corresponding author.
E-mail address: maximilian.schiester@unileoben.ac.at (M. Schiester).

https://doi.org/10.1016/j.surfcoat.2025.132879
Received 10 July 2025; Received in revised form 2 October 2025; Accepted 28 October 2025
Available online 2 November 2025
0257-8972/© 2025 The Author(s). Published by Elsevier B.V. This is an open access article under the CC BY license (http://creativecommons.org/licenses/by/4.0/).

occurrence of multiple detection events, i.e., more than one ion is detected within a single detection window of the ToF system [15–19]. These events are caused by the field evaporation itself, as neighboring surface atoms might evaporate together (i.e., correlated evaporation), often in bursts, during a voltage or laser pulse due to the non-uniform distribution of the electric field along terraces [20]. Also, the loss of undetectable neutrals through dissociation alters the measured stoichiometry, while complex molecular ions (e.g., Ti_2N) dissociate unpredictably during flight. Such dissociation eventually results in ion pile-up, i.e., the hardware limitation of the detector [6,21,22], despite improved detector design and advanced signal processing [23]. In addition, the mismatch in the evaporation fields of the species involved promotes preferential evaporation/retention, resulting in an over- and underestimation of the respective elements. This occurs because atoms with lower evaporation fields are more likely to be field-evaporated and detected, while others may be retained followed by burst evaporation and thus lead to compositional inaccuracies in the reconstructed data [24–26]. Recent developments in instrumentation show that shorter laser wavelengths (i.e., deep UV, DUV) can enhance the elemental accuracy for TiN coatings by increasing the energy density together with smaller spot size and thus mitigate compositional biases [27]. However, for carbides increasing discrepancies in the elemental composition are observed when using a DUV laser, presumably due to different laser-matter interactions [28].

Ion correlation histograms are an exceptional tool to investigate the occurrence of compositional biases [29]. The mass-to-charge state (m/n) ratios of individual ion pairs within the multiple detection events constitute the data points. This representation results in characteristic tracks, allowing co-evaporation or molecular dissociation to be studied. Additionally, the field evaporation conditions can be optimized by reference to the features exhibited in the ion correlation histogram. An alternative type of visualization is the ToF correlation histogram of individual ion pairs. In the work by Kruska and Schreiber [30], data could be successfully recovered from the APT background signal for oxides by analyzing out-of-sync co-evaporation, thus improving the elemental composition. Caplins *et al.* [31] presented the different cases of synchronous and out-of-sync evaporated single and multiple detection events. While single detection events, which are not synchronously evaporated with a voltage or laser pulse, are truly lost as randomized background, valuable information might be obtained from the background of multiple detection events. By analyzing multiple detection events, it is demonstrated that ToF differences between co-evaporated ion pairs in the background reveal distinct differences in ToF (ΔToF) peaks. As shown in Fig. 1, ΔToF is characteristic for an out-of-sync co-evaporated multiple detection event, independent of their absolute ToF values. This characteristic challenges the assumption that background signals are entirely random and instead shows that certain hits can be consistently identified. Hence, this approach could provide deep insights into the fundamental mechanisms governing field evaporation, allowing the identification of material-specific evaporation phenomena and their contribution to compositional biases. Differences in the evaporation behavior between the materials, such as the proportion of multiple detection events or molecular ions, also allow conclusions to be drawn about the different material properties, as these are significantly influenced by the nature of the chemical bond [32].

In the present work, significant differences between the field evaporation behavior of nitrides and carbides are highlighted, shedding light on how factors like preferential evaporation/retention, molecular dissociation, and joint delayed evaporation shape the measured composition. Distinguishing between these mechanisms allows for a more accurate interpretation to understand deviations of certain elements from expected stoichiometry and refining our understanding of the physical processes underlying APT measurements. Chemically homogeneous TiC and TiN coatings serve as model coatings to demonstrate the feasibility of this methodological approach. By analyzing correlated background signals within multiple detection events, normally neglected data, insights into field evaporation mechanisms and compositional biases are provided. The out-of-sync co-evaporation analysis is utilized as a tool to raise awareness in the growing APT community about methodological limitations and interpretation challenges, particularly for non-metallic bound materials which typically exhibit significant amounts of multiple detection events [1].

2. Materials and methods

The TiN and TiC coatings investigated in this study were synthesized using thermally activated chemical vapor deposition (CVD) in an industrial-scale SCT600 TH reactor (Sucotec). Cemented carbide cutting inserts (76 wt.% WC, 12 wt.% Co and 12 wt.% mixed carbides) in SNUN geometry (according to ISO 1832) served as substrate material. The TiC coating was synthesized using a feed gas mixture of $TiCl_4$, C_2H_6, and H_2 at 885 °C and 100 mbar. The TiN coating was grown using a gas mixture of $TiCl_4$, N_2, H_2 and Ar at 920 °C and 160 mbar. For further details on the deposition process and fundamental coating characterization, see Refs.

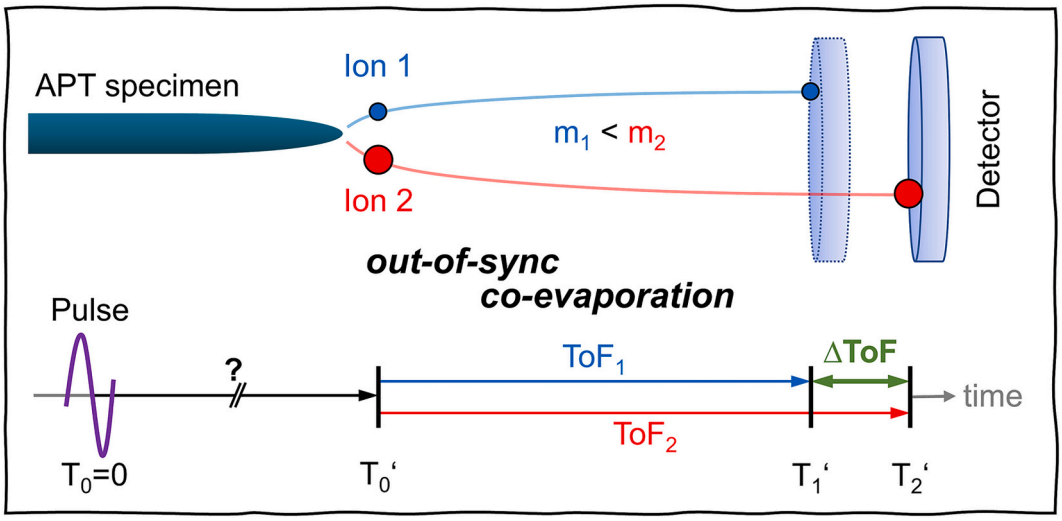


Fig. 1. Illustrated temporal sequence of out-of-sync co-evaporation with two ions. The mass of the first ion is smaller, resulting in a shorter ToF compared to the second ion. Due to the delayed co-evaporation at the unknown time T_0', the ΔToF is characteristic for this ion pair (ion 1 and ion 2) independent of their absolute ToF (T_1' and T_2').

[33, 34].

The elemental reference compositions were determined using time-of-flight elastic recoil detection analysis (ToF-ERDA) and complementary Rutherford backscattering spectrometry (RBS) as well as elastic backscattering spectrometry (EBS) at the 5 MV NEC Pelletron tandem accelerator facility, operated at the Tandem Laboratory of Uppsala University, Sweden [35]. For ToF-ERDA, I^{8+} primary ions applying 4 MV acceleration voltage resulting in a projectile energy of 36 MeV, for RBS and EBS He^{+} primary ions with 2 MeV and 4.5 MeV, respectively, were utilized. Systematic uncertainties for ToF-ERDA originate from the detection efficiency <1 for the light recoils C and N as well as the specific energy loss of primary ions and recoil species [36]. These uncertainties were minimized by using stoichiometric Cr_2AlC [37] and TiN [38] reference samples. Further information regarding this multi-method approach and associated uncertainties can be found in Ref. [39]. Depth profiles of TiC as well TiN were homogeneous and exhibited impurities of 0.3 at.% O and 0.5 at.% Cl (TiC) as well as 0.5 at.% O (TiN). Neglecting these impurities, the obtained reference elemental compositions were 49.3 ± 2.6 at.% Ti and 50.7 ± 2.6 at.% C for TiC and 49.4 ± 1.5 at.% Ti and 50.6 ± 1.5 at.% N for TiN. These numbers correspond, within the limits of 5 % (TiC) and 3 % (TiN) relative measurement uncertainty, to a stoichiometric composition.

Using a Struers Accutom 5R precision saw, ~400 μm thin sheets with the coated surface on top were cut. Following the procedure described by Tkadletz *et al.* [40], coupons with 15 pre-sharpened microtips were fabricated by fs-laser processing utilizing a 3D-Micromac microPREP PRO FEMTO laser micromachining tool (532 nm wavelength and ~ 230 fs pulse duration). Ready-to-run APT specimens were obtained by focused ion beam (FIB)-based standard routines including annular milling and a low kV clean-up [41] using an FEI Versa 3D DualBeam scanning electron microscope/Ga^{+}-FIB platform.

The APT measurements were conducted using two local electrode atom probes (LEAP) from CAMECA Instruments: a LEAP 5000 XR, equipped with a time-compensating reflectron (~52 % detection efficiency and 382 mm flight path) and a LEAP 5000 XS, featuring a straight flight path geometry (~80 % detection efficiency and 100 mm flight path). While the first offers an unprecedented mass resolving power, the latter profits from a very high detection efficiency. This advantageous combination of instruments allows to identify and compare differences caused by the flight path design in the out-of-sync co-evaporation evaluation. In the following, the LEAP 5000 XR and LEAP 5000 XS instrument platforms are referred to as XR and XS instrument, respectively, for reasons of brevity. Data sets, containing ~20 million ions, were acquired at 50 K base temperature in laser-assisted mode, applying 30 pJ laser pulse energy (UV laser with 355 nm wavelength and 10 ps pulse duration). The pulse rate was set to 250 kHz, while maintaining a detection rate of 1 %. During acquisition, the Ti^{3+}/Ti^{2+} charge state ratio (Ti-CSR) was recorded for the purpose of electric field strength estimation. The voltage-based reconstructions were carried out using the embedded IVAS module within the AP Suite 6.3 software environment by CAMECA Instruments. The ion assignment was performed following a symmetrical peak ranging approach, i.e., the peak onset from the background defined the start and the position of the peak maximum the center of the range [42]. Impurities of Ga, Cl and O were identified, however, since their total contribution is <1 at.%, they were deliberately excluded and thus, the elemental composition was normalized to the sum of the Ti, C and N contents. In the TiC dataset acquired with the XS instrument, a grain boundary was discernible due to minor Co decoration from the cemented carbide substrate, which is commonly observed in CVD TiCN coatings [43] and was considered negligible. The mass spectra of all measurements analyzed within this work (Fig. S1-S4) and an overview of the assigned ion species, the observed charge states, and the corresponding peak positions (Table S1 and S2) can be found in the supplementary material (section S1). Customized Python-based (3.12) software was utilized to analyze the *. EPOS files for multiplicity, ion pair distances, correlation histograms and out-of-sync co-evaporation behavior.

3. Results and discussion

3.1. Field evaporation behavior analysis

The observed global compositions for TiC and TiN measured with the XR and XS atom probe platforms and the corresponding C and N deviations from the ToF-ERDA/RBS/EBS reference compositions are summarized in Table 1. Errors due to counting statistics were calculated based on Poisson statistics for 20 million detected ions per dataset, yielding element-specific uncertainties between ±0.01 at.% and ± 0.02 at.% (detection efficiency was not considered). These errors are negligible compared to the observed uncertainties associated with ToF-ERDA/RBS/EBS. In all cases, an overestimation of the Ti content by APT is evident, which is in good agreement with previous works [4,6,10]. However, while the −2.3 at.% deviation of the nitride using the XR instrument only slightly exceeds the ±1.5 at.% uncertainty of ToF-ERDA/RBS, a detailed analysis is required to clarify the high inaccuracy of −11.7 at.% C deviation for the carbide compared to ±2.6 at.% uncertainty from ToF-ERDA/EBS. With the XS instrument, the deviation of N by −2.4 at.% for TiN is very similar to the XR instrument, while the composition for TiC becomes even more inaccurate with −16.9 at.% C deviation from the reference composition.

The probability of molecular ions (PMI) is also shown in Table 1 and corresponds to the proportion of evaporated ions consisting of more than one atom [32]. There are remarkable differences between TiC and TiN: While low PMI values of 9.6 (XR) and 12.7 % (XS) can be determined for the carbide, molecular ions represent the majority of the evaporated species in the nitride with 54.4 (XR) and 57.1 % (XS). For both materials the PMI values are ~3 % higher for the XS compared to the XR instrument. Speculating about possible reasons, the almost four times longer flight time (382 mm flight path length compared to 100 mm) in the XR instrument may allow for dissociation of the metastable molecular ions before reaching the detector. Moreover, the molecular ions might interact with the electric field of the reflectron in the XR instrument. Due to the limited statistics, premature conclusions should be taken with caution.

Kingham's post-ionization model [44] is used to estimate the field evaporation conditions. Detailed information on the approach can be found in Ref. [45]. The average Ti-CSRs for TiC are 0.37 (XR) and 0.15 (XS), which corresponds to an electric field strength at the apex of 38.8 and 37.4 V/nm, respectively. For TiN, slightly higher Ti-CSRs of 0.55 (XR) and 0.47 (XS) are observed, which results in an estimated electric field strength of 39.3 and 39.1 V/nm. For both coatings, the observed field strengths are lower when using the XS instrument, but it should be explicitly mentioned at this point that Kingham's model allows only estimates and the results should be treated with caution especially for non-metal containing materials.

Fig. 2(a) compares the ion multiplicity for TiC and TiN using the XR instrument and shows that both materials exhibit a similar exponential decline with increasing number of ions detected per event: TiC exhibits a slightly higher fraction of single events, while TiN shows an increased fraction at higher multiplicities. The corresponding detector distance

Table 1
Elemental compositions of TiC and TiN observed by the two instrument platforms, XR and XS, the corresponding deviations from the ToF-ERDA/RBS/EBS reference compositions as well as the probability of molecular ions (PMI) as observed within the mass spectra.

		Ti [at.%]	C [at.%]	N [at.%]	(C,N) deviation [at.%]	PMI [%]
TiC	XR	61.0	39.0	—	−11.7	9.6
	XS	66.2	33.8	—	−16.9	12.7
TiN	XR	51.7	—	48.3	−2.3	54.4
	XS	51.8	—	48.2	−2.4	57.1

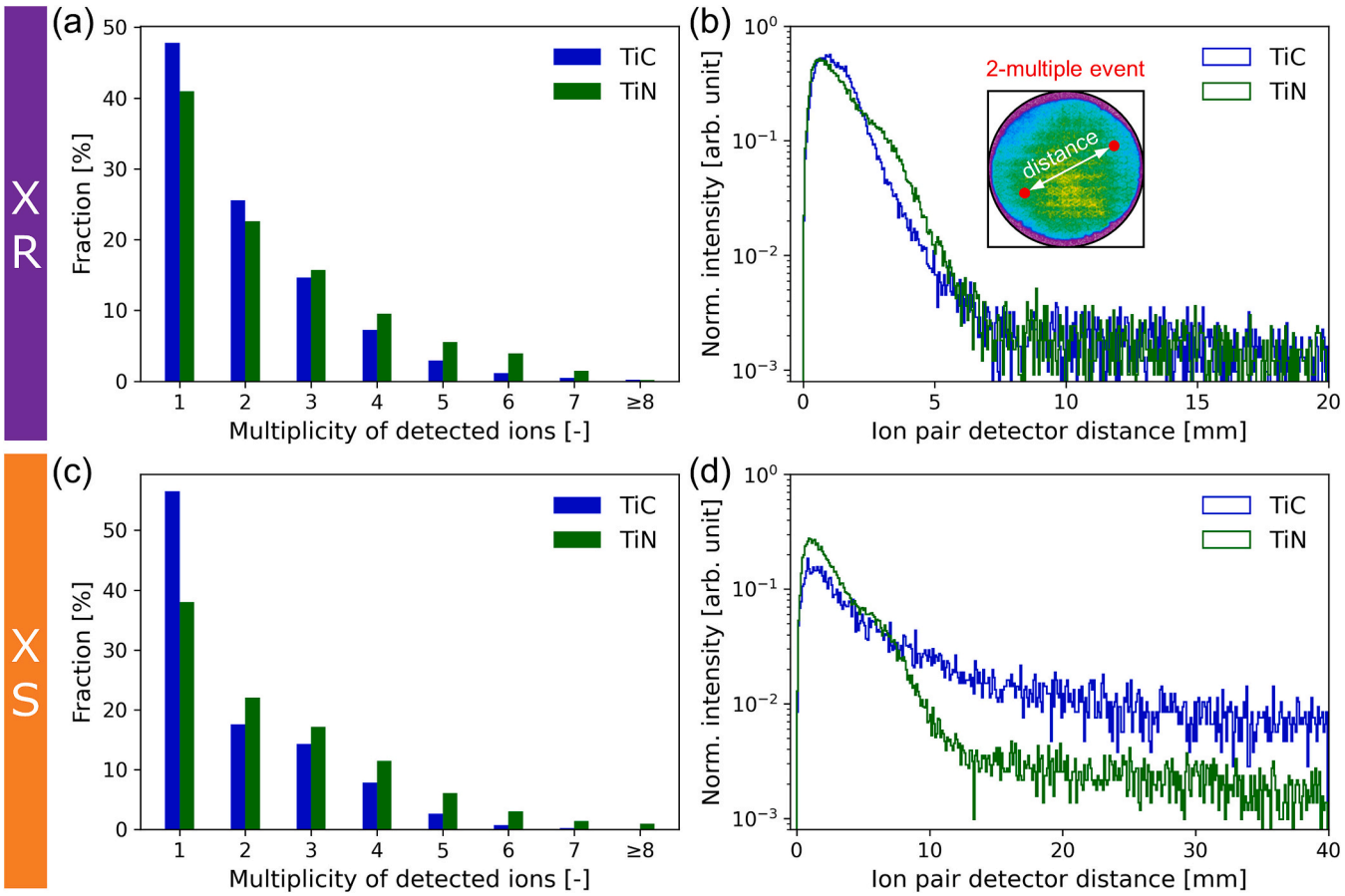


Fig. 2. Multiplicity of the detected ions and the detector distances of ion pairs within the 2- and 3-multiple detection events, visualized in a normalized histogram (0.05 mm binning), for TiC and TiN acquired with the (a-b) XR and (c-d) XS atom probe platform, respectively. An ion pair distance of a 2-multipe event is exemplified on the detector hit map of TiN in the inset of (b).

distributions for ion pairs from 2- and 3-multiple detection events are shown in Fig. 2(b). For both materials, the distances follow a similar trend: a sharp peak at short distances followed by an exponential decay. This behavior indicates evaporation from adjacent sites [46]. Undesired DC evaporation can be excluded from this type of distribution, as the ion pair distances would be spread over the entire detector in this case [9].

For the XS instrument, the ion multiplicity behavior of TiC and TiN is clearly different, as can be seen in Fig. 2(c): While for TiN the proportion of single detection events is slightly lower than with the XR instrument, for TiC it rises to well over 50 %. Since the acquisition parameters and field evaporation conditions are identical, these differences can be attributed mainly to the higher detection efficiency of the XS instrument. The increased flight path length, the interaction with the reflectron and the smaller detector area of the XR instrument result in the detection of merely 52 % of all evaporated ions and thus a considerable loss of information. Due to the larger detector area, the ion pair distances of the XS measurements in Fig. 2(d) are distributed over a broader range, accompanied by lower normalized intensities utilizing the same binning of the histogram. Here, distinct differences appear between the materials: TiC shows a broader distribution with a slower decay and a pronounced long-distance tail, pointing to a higher prevalence of co-evaporation from spatially distinct surface sites. In contrast, TiN shows a sharper peak at short distances and a steeper decline, comparable to the XR distribution. These observations in the intensity distribution, visible in Fig. 2(d), suggest considerable differences in field evaporation mechanisms between TiC and TiN.

A comparison of the ion pair detector distance distributions of multiple detection events with successive (i.e., consecutive) single detection events can be found in Fig. S5 of the Supplementary material (section S2). Considering the first maximum, which corresponds to evaporation from adjacent sites, there are differences between the single and multiple detection events visible: For TiN, a peak shoulder can be observed in the distribution of the multiple detection events for both instruments, which indicates larger distance and thus suggests the presence of dissociation processes [47]. The Coulomb repulsion of the positively charged fragments (also known as kinetic energy release [21,48]) results in larger distances. In case of TiC, the multiple detection events of the XS measurement show a broad distribution, which indicates joint evaporation from adjacent sites and/or molecular dissociation.

3.2. *Ion correlation histograms*

To investigate differences in field evaporation, ion correlation histograms were derived from 2- and 3-multiple events. For each event, all possible ion pair permutations were considered (e.g., for a 3-multiple: 1–2, 2–3, and 3–1). The data were further separated into ranged and background hits according to the applied range file. Fig. 3(a) and (b) show the ion correlation histograms for TiC using the XR and XS instrument, respectively, where distinct tracks become visible: Dense crossings (grid-like patterns) indicate synchronous (i.e., during a laser pulse) co-evaporation, resulting in proper detection. Horizontal and vertical tracks imply the occurrence of partly delayed evaporation, where one ion is evaporated with pulse and the other with a certain delay. Depending on the delay, the latter ion might be detected as background hit. Tracks with a positive gradient are of great interest within this work as they represent out-of-sync co-evaporation.

As illustrated in Fig. 1, the actual time of evaporation of both ions remains unknown (T_0') and therefore their m/n ratio is not correctly

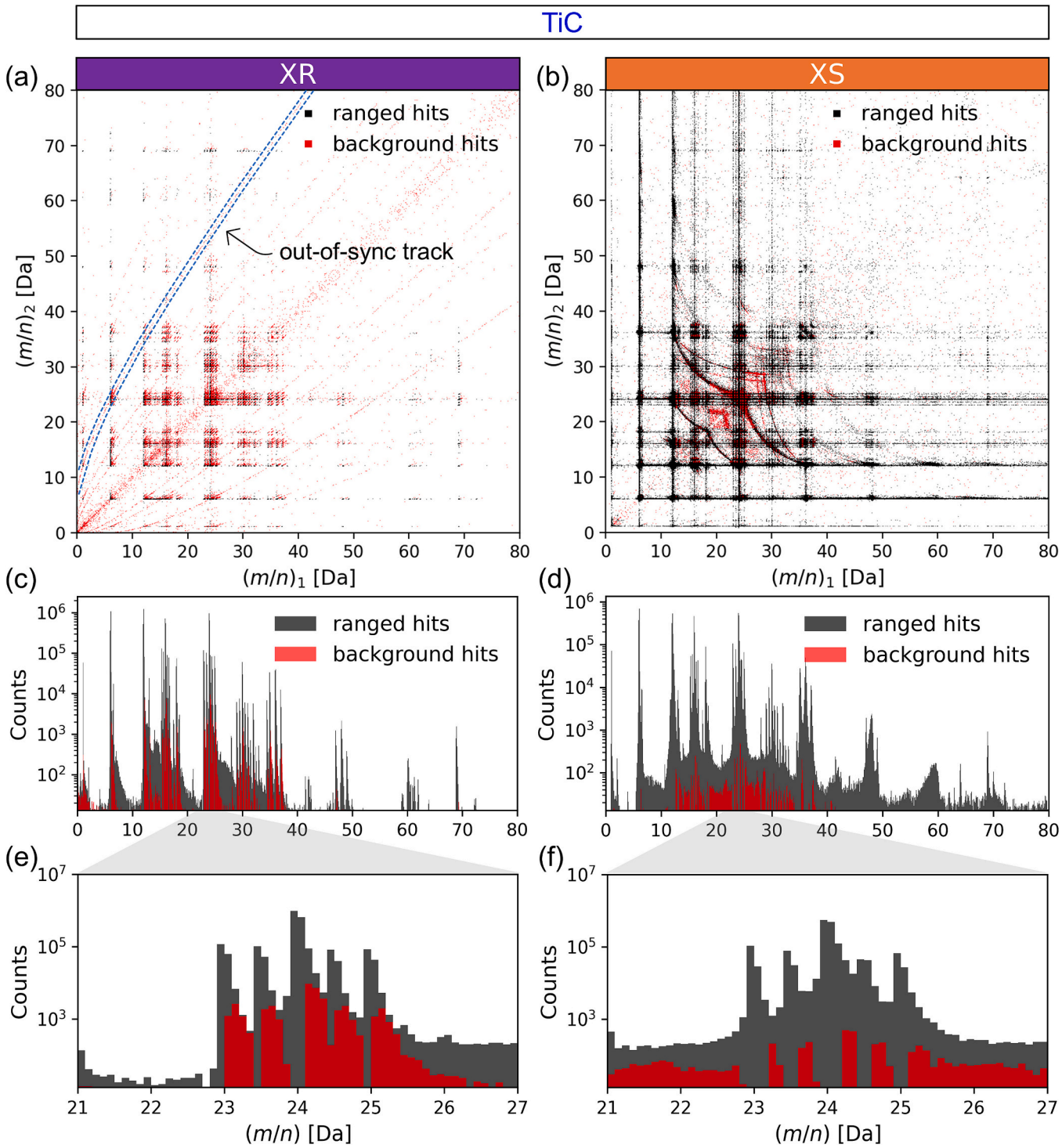


Fig. 3. (a-b) Ion correlation histograms, (c-d) the corresponding mass spectra (0.1 Da binning) derived from 2- and 3-multiples and (e-f) the Ti^{2+} peaks shown in detail for TiC, acquired with the XR and XS atom probe platform. The hits were separated in ranged and background hits according to the ranging applied to the mass spectra. Exemplarily an out-of-sync track exhibiting a positive slope is highlighted in (a).

determined. Due to their delay, usually both ions contribute to the background. For the evaluation of out-of-sync co-evaporation, only true background multiple detection events are considered, i.e. none of the ions within a detection event is assigned to an ion range in the mass spectrum. It should be noted that the number of true background hits depends directly on the operator and the selected ranging approach. Thus, ions detected within non-ranged thermal tails are not part of the reconstruction, but contribute to the out-of-sync co-evaporation evaluation as delayed evaporated hits and are therefore not lost. Significant differences can be seen between the two instruments: The tracks all appear weaker in the case of the XR; however this is due to the principle of the reflectron, which corrects small differences in the ToF and thus increases the mass resolving power (i.e. narrower peaks in the mass spectrum). The non-compensated broader peaks in the XS mass spectrum cause pronounced and connected tracks in the ion correlation histogram. The co-evaporation tracks with a positive slope are only

clearly visible in the case of the XR, which can be attributed to the broader peaks and thus, a lower amount of true background hits. However, only the histogram of the XS exhibits tracks with a negative slope, which is related to the presence of molecular dissociation [29,49].

Non-metallic compounds often evaporate as metastable molecular ions with short lifetimes. These can dissociate in flight into ionic or even neutral fragments. This phenomenon causes a compositional bias, since neutrals are not detected and fragments may be lost due to detector ion pile-up [23]. Using the XR instrument, the position of dissociation is decisive for the visibility of the corresponding dissociation track within the ion correlation histogram [48]. In the case of TiC, measured with the XR, the dissociation most likely occurs between the specimen and before entering the reflectron and thus, proper detection is impeded by the latter. In the course of this work, primarily dissociation processes can be observed in which a C^+ ion is formed during the decay of the parent molecule. This is in excellent agreement with the study by Peng *et al.*

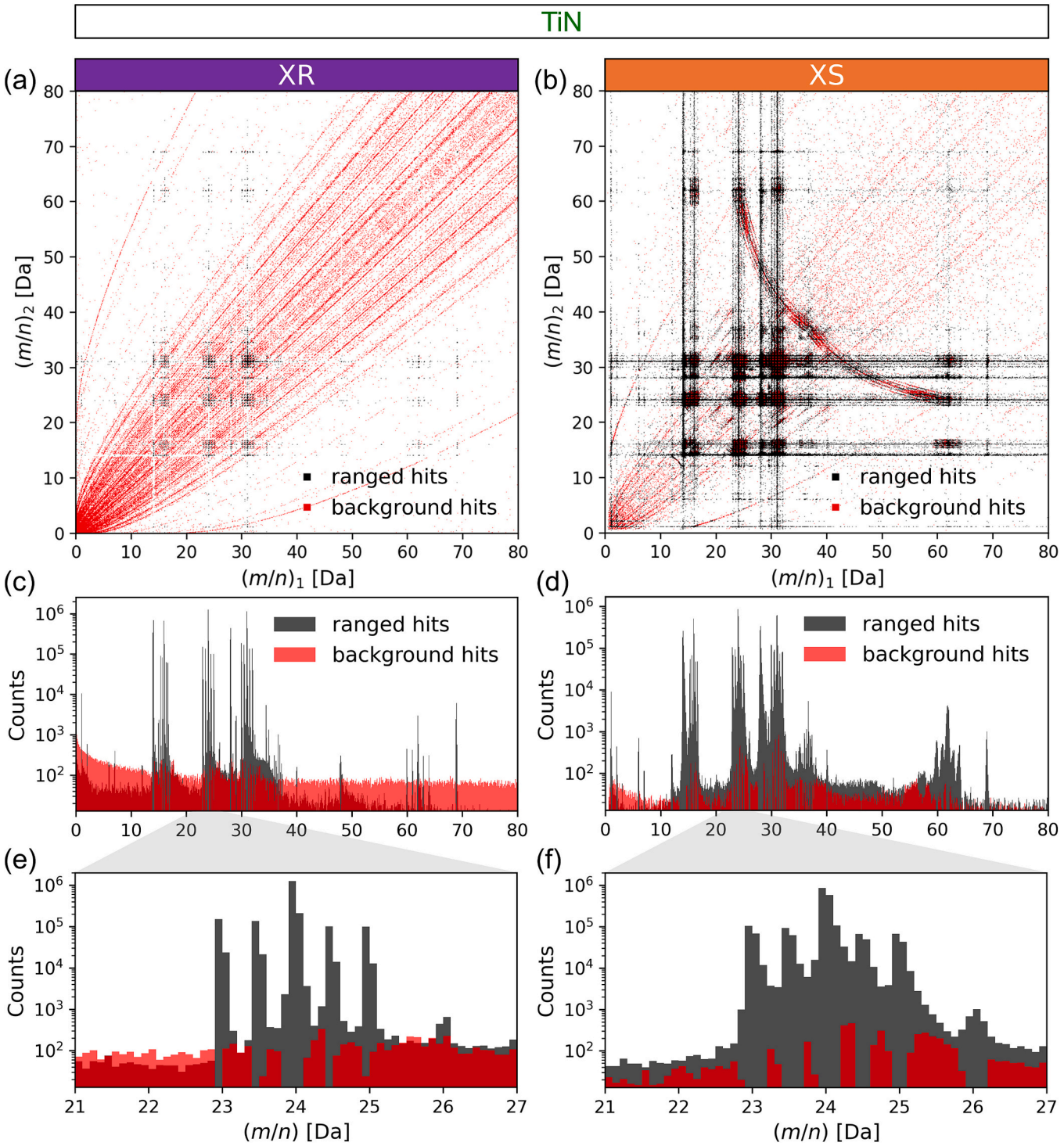


Fig. 4. (a-b) Ion correlation histograms, (c-d) the corresponding mass spectra (0.1 Da binning) derived from 2- and 3-multiples and (e-f) the Ti^{2+} peaks shown in detail for TiN, acquired with the XR and XS atom probe platform, respectively. The hits were separated in ranged and background hits according to the ranging applied to the mass spectra.

[21]. A detailed description and an overview of all identified dissociation tracks of TiC can be found in the supplementary material (section S3, Table S3 and Fig. S6).

The mass spectra derived from the ion correlation histograms are shown in Fig. 3(c) and (d). The detailed views of the Ti^{2+} peak regime (23–25 Da) in Fig. 3(e) and (f) impressively show the influence of the reflectron: The spectrum of the XR exhibits very sharp peaks, whereas that of the XS shows broad peaks accompanied by a low signal-to-noise ratio. Due to the increased peak width, the number of true background multiple detection events is considerably reduced for the latter. In general, it can be observed for TiC that the background hits occur locally between the peaks, in the case of the XR primarily as thermal tails. The mean background levels of the data sets are 8.0 (XR) and 10.0 (XS) ppm/ns.

Fig. 4(a) and (b) shows the ion correlation histograms for TiN represented by the 2- and 3-multiples acquired with the XR and XS instruments, respectively. At first glance, the more pronounced out-of-sync co-evaporation tracks extending from the origin with a positive slope are noticeable for both flight path designs. Similar to the carbide, the XS data set shows dense crossings, which seem to be compensated in the case of the XR. One dissociation track (negative slope) can also be identified for the nitride with the XS instrument: Dissociation of the type $Ti_2N^{3+} \rightarrow TiN^{+} + Ti^{2+}$ was already demonstrated with an XR instrument in an earlier work, however, only with the use of rather high laser pulse energy [6].

The corresponding mass spectra in Fig. 4(c) and (d) and the detailed views of the Ti^{2+} peak regime in Fig. 4(e) and (f) again illustrate the different mass resolving power of the instruments: Narrow peaks in the XR and wider peaks in the XS data set. The proportion of true background hits is significantly higher in the case of the XR than in that of the XS, which can be traced back to the increased width of the peak ranges in the mass spectrum of the XS measurement. The distribution of these background hits is noteworthy: In contrast to TiC, these are spread across the entire mass spectra and exhibit a constant level in the XR data set. This is in good agreement with the significant amount of out-of-sync co-evaporation observed in the ion correlations histograms for TiN and in accordance with an elevated average background level of 18.5 (XR) and 12.5 (XS) ppm/ns. Furthermore, there are no indications for pronounced thermal tails in the mass spectrum of TiN.

The different intensities of the out-of-sync tracks in the ion correlation histograms of TiC and TiN require profound analyses to further uncover the material-dependent differences in field evaporation behavior.

3.3. Out-of-sync co-evaporation of TiC

ToF correlation histograms are well suited for further analysis, as co-evaporated ion pairs appear as linear tracks due to their constant ΔToF [30,31]. Corrected ToF values, after voltage and flight path correction, from 2- and 3-multiple events were used for this purpose. The ToF correlation histograms for TiC are provided in the supplementary material (Section S4, Figs. S7 and S8). From these histograms, out-of-sync correlation plots can be derived, which form the core of this study. Here, the ΔToF of all ion pairs is visualized as a histogram. Alternatively, the difference between the square roots of the m/n ratios ($\Delta\sqrt{m/n}$) can be used [29]. In this work, $\Delta\sqrt{m/n}$ was chosen, as peak identification is more intuitive, as shown in Fig. 5 for TiC measured with the XR instrument.

However, both synchronous and out-of-sync co-evaporated ion pairs cause peaks, as ΔToF is constant in both cases. Therefore, it is necessary to correlate the $\Delta\sqrt{m/n}$ data points with the corresponding m/n values (see Fig. 5, bottom panel). While out-of-sync co-evaporation can be observed by tracks with positive slope in ion correlation histograms (see Fig. 3 and 4), they appear as vertical tracks in out-of-sync correlation

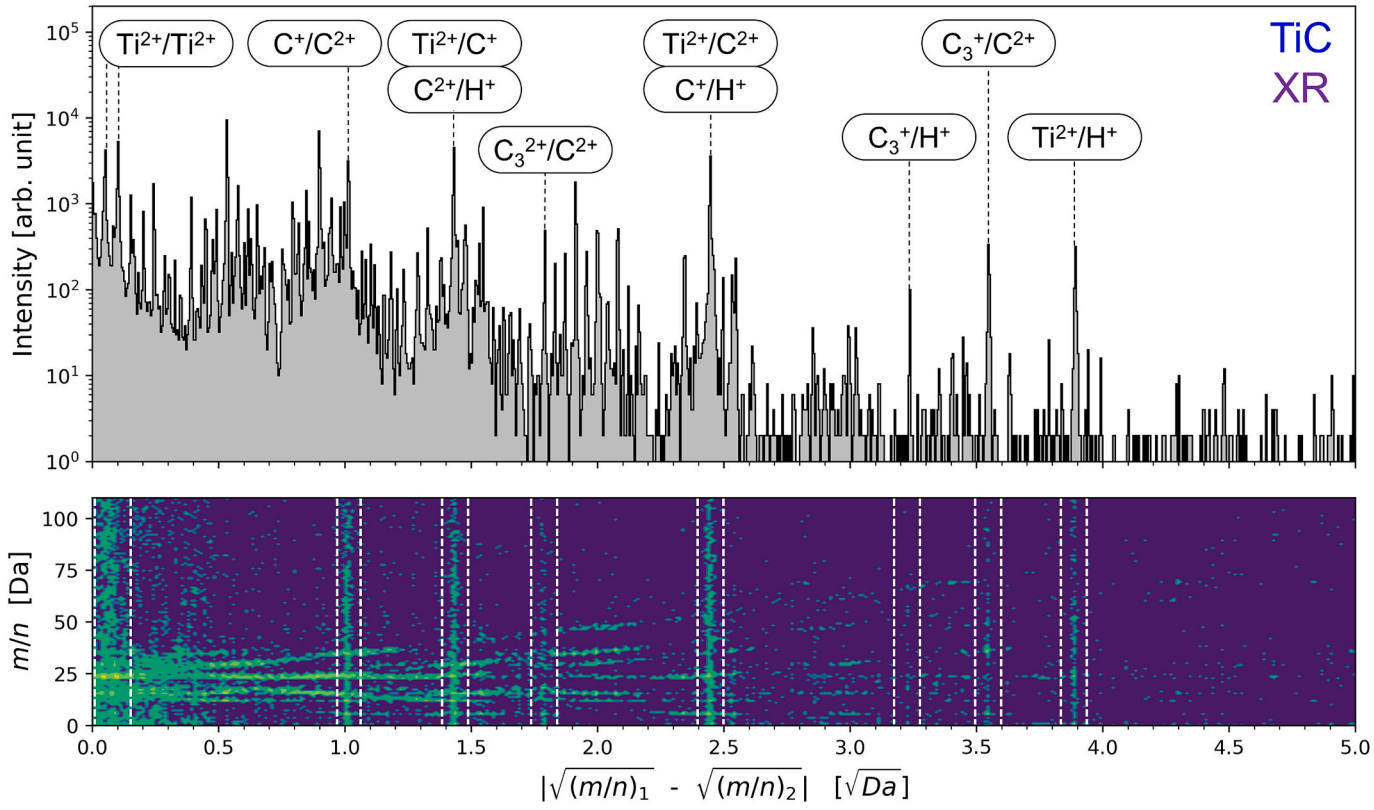


Fig. 5. Out-of-sync correlation plot for TiC, measured with the XR instrument. Identified vertical tracks are highlighted with white dashed vertical lines in the m/n scatter plot and the corresponding ion pairs are labelled in the histogram. Instead of corrected ToF difference, the proportional difference between the roots of the m/n-ratio roots within the 2 and 3-multiples was utilized. For the histogram a binning of 0.005 $\sqrt{Da}$ was employed.

plots since the corrected and detected ToF in general do not coincide. As a result, the hits generate data points scattered (vertically) over the entire mass spectrum. White dashed lines are employed to visually guide the vertical tracks of interest in Fig. 5. Synchronous co-evaporation results in defined horizontal tracks at constant m/n ratios, since the ToF of the ions is accurately determined.

In case of TiC, eight distinct peaks can be seen, to which the corresponding ion pairs could be allocated. The exact peak positions and species involved can be found in Table S4 in the supplementary material (section S5). Multiple detection events of the low field component Ti (theoretical evaporation field of 26 V/nm for elemental Ti in charge state 2+ [50]), seem to contribute to the background in the form of DC or preferential evaporation. Ion pairs in all possible permutations of the five Ti isotopes in charge state 2+ can be identified at low $\Delta\sqrt{m/n}$. Noticeably, carbon is involved in almost all ion pairs identified and thus not contributing to the elemental composition resulting in the pronounced underestimation of C. This observation in turn is in good agreement with the fact that carbon, as high field component, is retained and finally evaporates in the form of groups from adjacent sites [51].

To confirm this at the detector level, a spatially resolved analysis of out-of-sync co-evaporation was performed. For this purpose, the detector coordinates of selected ion pair peaks were extracted and, in addition to the detector heat map, a plot of the relative ion positions (i.e. their spatial distance) was generated. For high intensity peaks, features can be observed in the detector heat maps that may indicate crystallographic patterns. The relative ion position maps show dense and concentrated patterns in the center, confirming evaporation from adjacent sites and no random distribution. The spatially resolved analyses for TiC (XR) are shown in Fig. S11 and S12 in the supplementary material (section S6).

Carbon possesses a major isotope (^{12}C) with a high natural abundance (98.89 %) [52]. As a result, the probability of ion pile-ups at the detector is very high, causing a strong underestimation of the C content, as also observed in this work [4]. Within this study, a pronounced ion pile-up can be observed for both measurements using the XR and the XS instrument utilizing the ^{13}C method [51]. The analysis and correction of the elemental composition are described in the supplementary material (section S7, Table S6 and S7). A possible peak overlap of Ti^{2+} with C_2^+ at 24 Da could be excluded based on the isotopic ratios of Ti^{2+}. Ti^{2+}/H^+ exhibits the largest $\Delta\sqrt{m/n}$, which is due to the large difference in masses. The hydrogen stems most probably from the residual gas remaining within the analysis chamber and is field desorbed together with Ti.

In addition to vertical tracks, clear horizontal tracks with well-defined m/n ratios are visible. These originate from thermal tails that were not fully ranged and indicate synchronous co-evaporation of two species. The tracks mainly consist of TiC and Ti, which evaporate together for all isotopes. While this analysis also provides insights into field evaporation behavior, it is beyond the scope of this work.

The analysis of the out-of-sync evaporation for TiC is also feasible with the XS instrument, as can be seen in Fig. 6 for TiC. However, there are some differences visible, which are primarily due to the lower mass resolving power compared to the XR: The peaks are not as intense, exhibit a lower signal to noise ratio (where noise belongs to uncorrelated evaporation) and are significantly broader. On the one hand, the wider peak ranges in the mass spectrum result in a reduced number of true background hits, as there is less space between ranges for background signals to occur. On the other hand, small differences in the kinetic energy, and thus ToF, are not compensated for, which results in broader peaks. Despite this, the same major peaks can be identified (cf. Fig. 5), which can be assigned to the ion pairs involving the respective major isotopes. Besides the co-evaporation of Ti^{2+} of its own isotopes, no distinct patterns of involved isotopes can be identified.

In general, the vertical out-of-sync co-evaporation hits are scattered over a wider range of m/n ratios, which is due to the shorter flight path

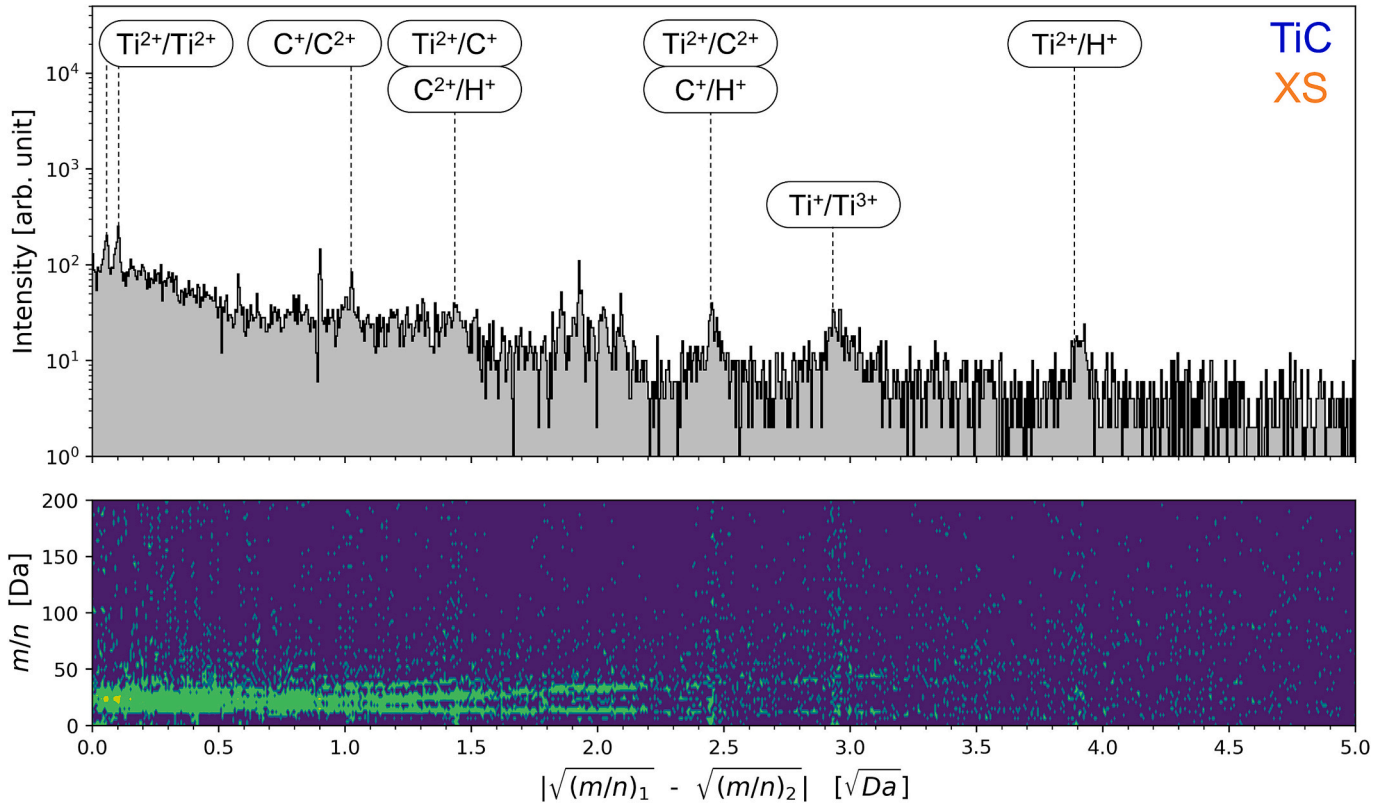


Fig. 6. Out-of-sync correlation plot for TiC, measured with the XS instrument. Identified vertical tracks are only labelled and deliberately not highlighted to enhance clarity. Instead of corrected ToF difference, the proportional difference between the m/n-ratio roots within the 2-multiples was utilized. For the histogram a binning of 0.005 $\sqrt{Da}$ was employed.

of the XS atom probe (100 mm) compared to the XR atom probe (382 mm), resulting in ions of the same species exhibiting a shorter ToF (see also ToF correlation histograms for TiN in the supplementary material, section S4, Fig. S9 and S10). The same pulse frequency (250 kHz in this work) results in an equally long detection window, which in the case of the XS allows the detection of larger m/n ratios at same standing voltage.

3.4. Out-of-sync co-evaporation of TiN

The out-of-sync correlation plot for TiN using the XR instrument in Fig. 7 differs considerably from that of TiC. As expected from the ion correlation histogram and the corresponding mass spectrum (cf. Fig. 4a and c), there are significantly more and intense vertical tracks present in case of TiN. For reasons of clarity these were not individually highlighted. A precise overview with the peak positions and species involved can be found in Table S5 the supplementary material (section S5).

The five isotopes of Ti result in characteristic patterns in this representation, similar to those in the mass spectrum. In addition to the out-of-sync co-evaporation of Ti with its own isotopes already known from TiC, it is noticeable that a variety of molecular ions are involved in the case of TiN. Primarily, ion pairs with TiN^{2+} can be observed with all other species (i.e., Ti^{2+}, Ti^{3+}, N^{+}, N_2^{+} and H^{+}). A possible reason might be that nitrides have a particular tendency to evaporate in the form of molecular ions, as also observed within this work by high PMI values >50 %, an effect that might be linked to differences in the bonding mechanisms between the materials [32]. These numerous tracks make it difficult to fully identify further out-of-sync co-evaporation tracks, thus it should be noted that there may be other hidden tracks between 0 and 2 $\sqrt{Da}$. For large differences, ion pairs could be identified with H^{+} and, in contrast to TiC, also with molecular H_2^{+}. This H is again most probably stemming from the residual gas as the reference composition obtained by ToF-ERDA/RBS did not reveal significant H content. Horizontal tracks resulting from synchronous co-evaporation are neglectable compared to TiC. This absence of synchronous co-evaporation indicates significantly different field evaporation mechanisms.

Considering the elemental accuracy, the losses of Ti and N in the form of background hits are relatively balanced in contrast to TiC, which is in good agreement with the smaller deviation from the ToF-ERDA/RBS/EBS reference compositions. Also for TiN, the spatially resolved analysis of out-of-sync co-evaporation revealed regions of higher intensity and symmetric features in the detector heat maps. The relative ion position maps prove again co-evaporation from adjacent sites without evidence for a random distribution of these true background hits. The plots can be seen in Figs. S13-S15 in the supplementary material (section S6).

By switching from the XR to the XS instrument, TiN shows similar differences in the analysis of out-of-sync co-evaporation as TiC: The intensity and the signal-to-noise ratio decrease considerably and the peaks become significantly broader, as can be seen in Fig. 8. Although the same main peaks are recognizable, many of them have lost their characteristic patterns by the involved isotopes. These findings can again be attributed to the reduced mass resolving power of the XS instrument. In contrast to the XR instrument, horizontal tracks can be seen indicating synchronous co-evaporation. While some ion pair peaks are no longer visible due to the circumstances mentioned above, there is a new, very clear peak at ~2.95 $\sqrt{Da}$: This is presumably a superposition of two peaks caused by the ion pairs Ti^{+}/Ti^{3+} and TiN^{+}/Ti^{2+}. The latter is of particular interest, as it corresponds to the daughter ions of the observed dissociation process of Ti_2N^{3+}.

3.5. Quantitative assessment

Analogously to the background recovery approach by Kruska and

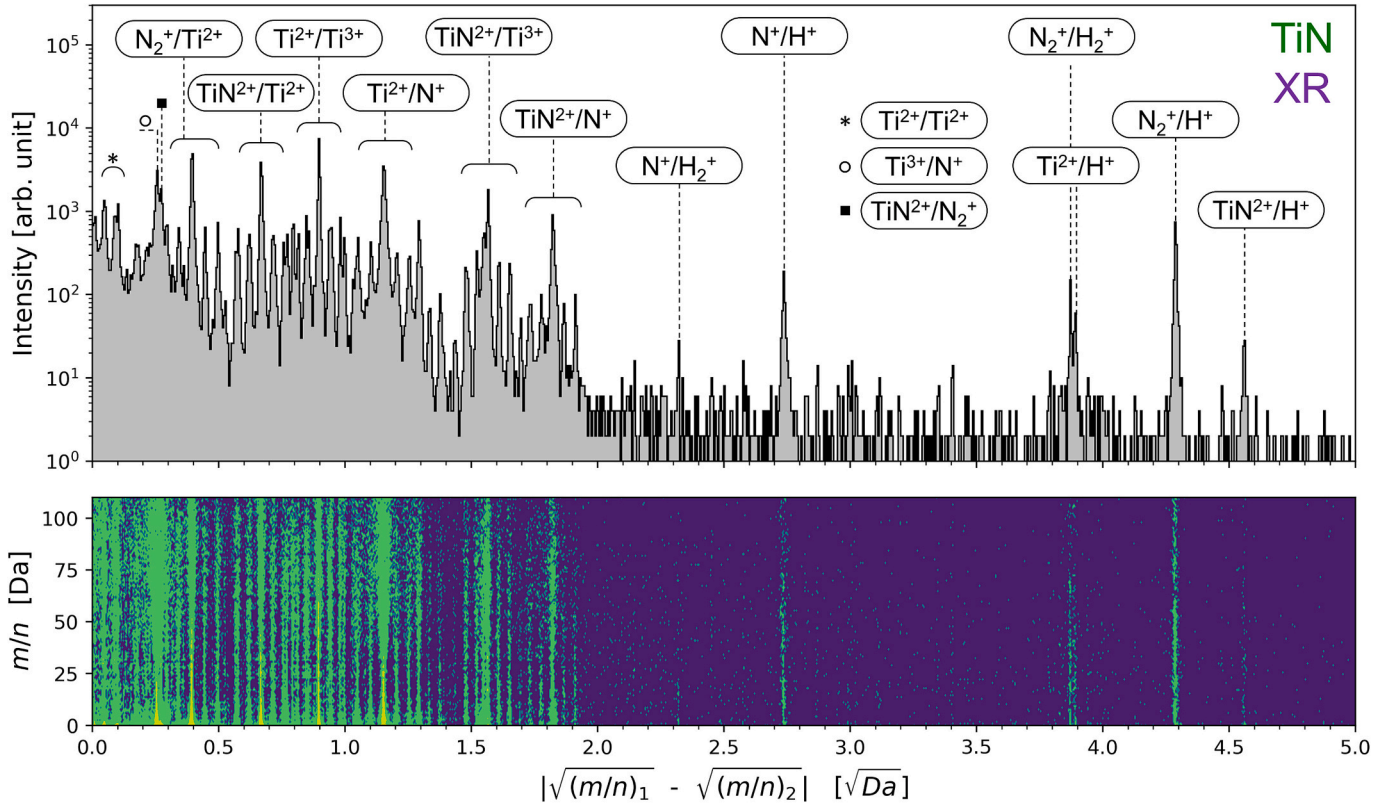


Fig. 7. Out-of-sync correlation plot for TiN, measured with the XR instrument. Identified vertical tracks are only labelled and deliberately not highlighted to enhance clarity. Instead of corrected ToF difference, the proportional difference between the m/n-ratio roots within the 2-multiples was utilized. For the histogram a binning of 0.005 $\sqrt{Da}$ was employed.

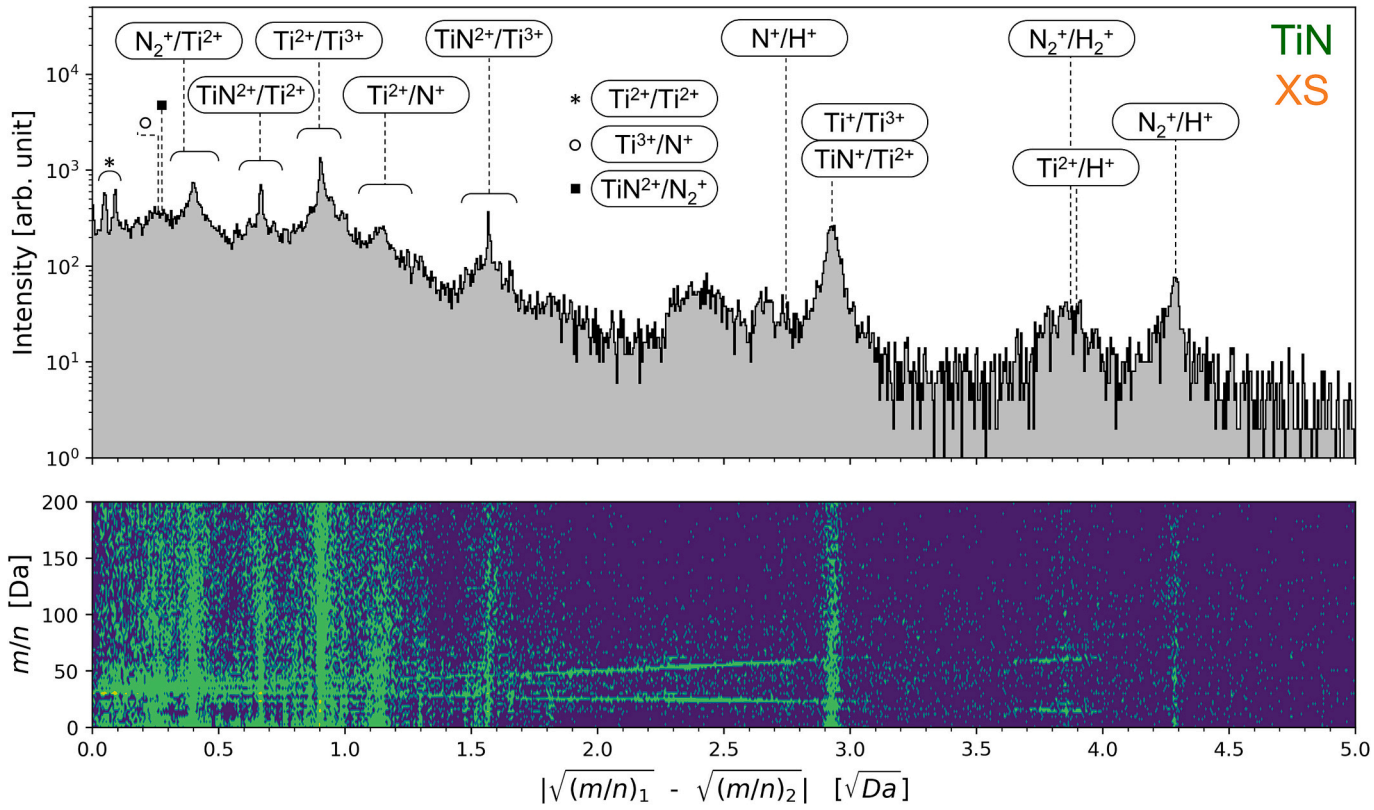


Fig. 8. Out-of-sync correlation plot for TiN, measured with the XS instrument. Identified vertical tracks are only labelled and deliberately not highlighted to enhance clarity. Instead of corrected ToF difference, the proportional difference between the m/n-ratio roots within the 2-multiples was utilized. For the histogram a binning of 0.005 $\sqrt{Da}$ was employed.

Schreiber [30], the number of out-of-sync co-evaporated ion pairs of the identified ion pairs was determined in this work. For this purpose, the counts in the corresponding $\Delta\sqrt{m/n}$ peak ranges (see supplementary material, section S5) were summed up and assigned to the species. The number of recovered counts, the decomposed composition and the corresponding (C,N)/Ti ratio are summarized in Table 2. The results clearly show that the number of recovered counts of TiN significantly exceeds that of TiC for both instruments. This was to be expected due to the large number of tracks and molecular ions involved in the case of TiN. The XS instrument, however, yields notably fewer recovered counts due to its reduced signal-to-noise ratio and the absence of peaks from minor isotopes. Despite these limitations, a consistent trend is observed: the (C,N)/Ti ratio is always <1. Since the non-metallic fraction is underestimated in all APT measurements (see Table 1), the elemental accuracy cannot be improved directly by the recovered counts in any case. For both, TiC and TiN, this can most probably be attributed to the previously observed preferential evaporation of Ti. Furthermore, as Kruska and Schreiber have already described [30], the influence on the overall composition is very small due to the relatively low number of recovered 2- and 3-multiple detection events. Therefore, the analysis of out-of-sync co-evaporation primarily serves as a qualitative tool to identify compositional biases and guide the application of correction methods, such as the ^{13}C-based ion pile-up correction.

Table 2
Quantitative assessment of out-of-sync co-evaporation for TiC and TiN using the two different instrument platforms, XR and XS.

		Recovered counts [−]	Ti [−]	C [−]	N [−]	(C,N)/Ti [−]
TiC	XR	64,188	39,320	24,868	—	0.63
	XS	4436	3598	838	—	0.23
TiN	XR	235,502	136,918	—	98,584	0.72
	XS	40,418	27,628	—	12,790	0.46

4. Conclusions

This study provides new insights into compositional biases in atom probe tomography of transition metal carbides and nitrides by systematically analyzing the background for out-of-sync co-evaporation. The results indicate that compositional deviations in TiC and TiN are closely linked to differences in field evaporation behavior. Ion correlation histograms combined with detailed background analysis reveal that TiC exhibits distinct out-of-sync co-evaporation of ion pairs, alongside synchronous co-evaporation, most likely within thermal tails. In contrast, TiN shows a broader range of vertical correlation tracks and a stronger tendency for molecular ion formation, resulting in a considerable and more uniform background level. This is also corroborated by the PMI, since molecular ions constitute the majority of all ions in the mass spectrum of TiN (54.4–57.1 %), while for TiC significant lower values (9.6–12.7 %) were observed.

A direct comparison between the XR and XS platforms further highlights the instrumental impact on field evaporation analysis. The XR system, with its higher mass resolution due to the reflectron, enables more precise identification of out-of-sync co-evaporation, identification of isotopic patterns with a good signal-to-noise ratio. Meanwhile, the XS instrument offers increased detection efficiency, the ability to study dissociation phenomena and a broader field of view, though at the cost of peak broadening and reduced ability to resolve background contributions. Both flight path geometries are suitable for analyzing out-of-sync co-evaporation but exhibit device-specific characteristics.

The results underscore the potential of advanced background analysis as a complementary tool to refine atom probe quantification and provide a deeper understanding to the origin of multiple detection events. Incorporating such approaches into analysis strategies allows to

identify material-specific compositional biases and how acquisition parameters affect the field evaporation behavior. Crucially, the methodology and findings presented here assist in interpreting and mitigating compositional biases which represent a significant step toward improving measurement reliability for complex materials. Moreover, the utilized out-of-sync co-evaporation analysis bears potential to investigate pseudo multiple detection events, i.e. multiple evaporation events originating from the same pulse but recorded as successive singles due to exceeding the detector's detection window.

CRediT authorship contribution statement

Maximilian Schiester: Writing – original draft, Visualization, Software, Methodology, Investigation, Formal analysis, Conceptualization. **Marcus Hans:** Writing – review & editing, Investigation, Funding acquisition, Formal analysis. **Daniel Primetzhofer:** Writing – review & editing, Investigation, Formal analysis. **Jan Köttgen:** Writing – review & editing, Investigation, Formal analysis. **Christoph Czettl:** Writing – review & editing, Funding acquisition. **Nina Schalk:** Writing – review & editing, Supervision, Project administration. **Michael Tkadletz:** Writing – review & editing, Supervision, Project administration, Funding acquisition.

Declaration of Generative AI and AI-assisted Technologies in the Writing Process

During the preparation of this work the authors used ChatGPT (openai.com) in order to enhance clarity and readability. After using this tool, the authors reviewed and edited the content as needed and take full responsibility for the content of the published article.

Declaration of competing interest

The authors declare that they have no known competing financial interests or personal relationships that could have appeared to influence the work reported in this paper.

Acknowledgments

The authors want to thank Dr. Katherine P. Rice from CAMECA Instruments, United States and Prof. Lorenzo Rigutti from Université de Rouen Normandie, France for the fruitful discussions. We gratefully acknowledge Patrick Thelen from RWTH Aachen, Germany, for the experimental support. The financial support by the Austrian Federal Ministry of Labour and Economy, the National Foundation for Research, Technology and Development and the Christian Doppler Research Association is gratefully acknowledged. Financial support from the Austrian Research Agency (FFG) in the project "Future Matter by APT" (FFG-No. 884644) is also gratefully acknowledged. Transnational access to the ion beam analysis facility at Uppsala University has been supported by the RADIATE project under the Grant Agreement 824096 from the EU Research and Innovation program HORIZON 2020. Accelerator operation at Uppsala University has been supported by the Swedish Research Council VR-RFI (#2019-00191).

Appendix A. Supplementary data

Supplementary data to this article can be found online at https://doi.org/10.1016/j.surfcoat.2025.132879.

Data availability

Data will be made available on request.

References

[1] B. Gault, A. Chiaramonti, O. Cojocaru-Mirédin, P. Stender, R. Dubosq, C. Freysoldt, S.K. Makineni, T. Li, M. Moody, J.M. Cairney, Atom probe tomography, Nat. Rev. Methods Primers 1 (2021) 51, https://doi.org/10.1038/s43586-021-00047-w.
[2] S.H. Kim, S. Bhatt, D.K. Schreiber, J. Neugebauer, C. Freysoldt, B. Gault, S. Katnagallu, Understanding atom probe's analytical performance for iron oxides using correlation histograms and ab initio calculations, New J. Phys. 26 (2024), https://doi.org/10.1088/1367-2630/ad309e.
[3] S. Jakob, A. Fazi, M. Thuvander, Laser-assisted field evaporation of Chromia with deep ultraviolet laser light, Microsc. Microanal. (2024), https://doi.org/10.1093/mam/ozae111.
[4] M. Thuvander, D. Shinde, A. Rehan, S. Ejnermark, K. Stiller, Improving compositional accuracy in APT analysis of carbides using a decreased detection efficiency, Microsc. Microanal. 25 (2019) 454–461, https://doi.org/10.1017/S1431927619000424.
[5] M. Hans, J.M. Schneider, On the chemical composition of TiAlN thin films - comparison of ion beam analysis and laser-assisted atom probe tomography with varying laser pulse energy, Thin Solid Films 688 (2019) 137251, https://doi.org/10.1016/j.tsf.2019.04.026.
[6] M. Schiester, H. Waldl, M. Hans, M. Thuvander, D. Primetzhofer, N. Schalk, M. Tkadletz, Influence of multiple detection events on compositional accuracy of TiN coatings in atom probe tomography, Surf. Coat. Technol. 477 (2024) 130318, https://doi.org/10.1016/j.surfcoat.2023.130318.
[7] F. Meisenkothen, E.B. Steel, T.J. Prosa, K.T. Henry, R. Prakash Kolli, Effects of detector dead-time on quantitative analyses involving boron and multi-hit detection events in atom probe tomography, Ultramicroscopy 159 (2015) 101–111, https://doi.org/10.1016/j.ultramic.2015.07.009.
[8] Richard.J.H. Morris, R. Cuduvally, D. Melkonyan, C. Fleischmann, M. Zhao, L. Arnoldi, P. van der Heide, W. Vandervorst, Toward accurate composition analysis of GaN and AlGaN using atom probe tomography, J. Vac. Sci. Technol. B Nanotechnol. Microelectron. Mater. Process. Meas. Phenom. 36 (2018), https://doi.org/10.1116/1.5019693.
[9] E. Di Russo, I. Blum, J. Houard, M. Gilbert, G. Da Costa, D. Blavette, L. Rigutti, Compositional accuracy of atom probe tomography measurements in GaN: impact of experimental parameters and multiple evaporation events, Ultramicroscopy 187 (2018) 126–134, https://doi.org/10.1016/j.ultramic.2018.02.001.
[10] J. Angseryd, F. Liu, H.O. Andren, S.S.A. Gerstl, M. Thuvander, Quantitative APT analysis of Ti(C,N), Ultramicroscopy 111 (2011) 609–614, https://doi.org/10.1016/j.ultramic.2011.01.031.
[11] M. Hans, M. Tkadletz, D. Primetzhofer, H. Waldl, M. Schiester, M. Bartosik, C. Czettl, N. Schalk, C. Mitterer, J.M. Schneider, Is it meaningful to quantify vacancy concentrations of nanolamellar (Ti,Al)N thin films based on laser-assisted atom probe data? Surf. Coat. Technol. 473 (2023) 130020 https://doi.org/10.1016/j.surfcoat.2023.130020.
[12] N. Schalk, M. Tkadletz, C. Mitterer, Hard coatings for cutting applications: physical vs. chemical vapor deposition and future challenges for the coatings community, Surf. Coat. Technol. 429 (2022) 127949, https://doi.org/10.1016/j.surfcoat.2021.127949.
[13] W. Schintlmeister, O. Pacher, Preparation and properties of hard-material layers for metal machining and jewelry, J. Vac. Sci. Technol. 12 (1975) 743–748, https://doi.org/10.1116/1.568659.
[14] J.-E. Sundgren, Structure and properties of TiN coatings, Thin Solid Films 128 (1985) 21–44, https://doi.org/10.1016/0040-6090(85)90333-5.
[15] Z. Peng, F. Vurpillot, P.P. Choi, Y. Li, D. Raabe, B. Gault, On the detection of multiple events in atom probe tomography, Ultramicroscopy 189 (2018) 54–60, https://doi.org/10.1016/j.ultramic.2018.03.018.
[16] U. Rolander, H.-O. Andrén, On atom-probe analysis of cubic MX-type carbides and carbonitrides, J. Phys. Colloq. 49 (1988), https://doi.org/10.1051/jphyscol:1988652. C6-299-C6-304.
[17] Y. Chen, B. Geiser, E. Oltman, K. Rice, R. Ulfig, T. Prosa, Study of correlative evaporation and ion dissociation in atom probe data, Microsc. Microanal. 26 (2020) 2882, https://doi.org/10.1017/s1431927620023090.
[18] Z. Peng, P.P. Choi, B. Gault, D. Raabe, Evaluation of analysis conditions for laser-pulsed atom probe tomography: example of cemented tungsten carbide, Microsc. Microanal. 23 (2017) 431–442, https://doi.org/10.1017/S1431927616012654.
[19] L. Yao, B. Gault, J.M. Cairney, S.P. Ringer, On the multiplicity of field evaporation events in atom probe: a new dimension to the analysis of mass spectra, Philos. Mag. Lett. 90 (2010) 121–129, https://doi.org/10.1080/09500830903472997.
[20] F. De Geuser, B. Gault, A. Bostel, F. Vurpillot, Correlated field evaporation as seen by atom probe tomography, Surf. Sci. 601 (2007) 536–543, https://doi.org/10.1016/j.susc.2006.10.019.
[21] Z. Peng, D. Zanuttini, B. Gervais, E. Jacquet, I. Blum, P.P. Choi, D. Raabe, F. Vurpillot, B. Gault, Unraveling the Metastability of C_n^{2+} (n = 2-4) clusters, J. Phys. Chem. Lett. 10 (2019) 581–588, https://doi.org/10.1021/acs.jpclett.8b03449.
[22] U. Rolander, H.-O. Andrén, Statistical correction for pile-up in the atom-probe detector system, J. Phys. Colloq. 50 (1989) C8-529–C8-534, https://doi.org/10.1051/jphyscol:1989891.
[23] G. Da Da Costa, H. Wang, S. Duguay, A. Bostel, D. Blavette, B. Deconihout, Advance in multi-hit detection and quantization in atom probe tomography, Rev. Sci. Instrum. 83 (2012), https://doi.org/10.1063/1.4770120.
[24] C. Hatzoglou, S. Rouland, B. Radiguet, A. Etienne, G. Da Costa, X. Sauvage, P. Pareige, F. Vurpillot, Preferential evaporation in atom probe tomography: an analytical approach, Microsc. Microanal. 26 (2020) 689–698, https://doi.org/10.1017/S1431927620001749.

[25] J. Takahashi, K. Kawakami, A quantitative model of preferential evaporation and retention for atom probe tomography, Surf. Interface Anal. 46 (2014) 535–543, https://doi.org/10.1002/sia.5555.
[26] S. Ndiaye, C. Bacchi, B. Klaes, M. Canino, F. Vurpillot, L. Rigutti, Surface dynamics of field evaporation in silicon carbide, J. Phys. Chem. C 127 (2023) 5467–5478, https://doi.org/10.1021/acs.jpcc.2c08908.
[27] M. Schiester, H. Waldl, K.P. Rice, M. Hans, D. Primetzhofer, N. Schalk, M. Tkadletz, Effects of laser wavelength and pulse energy on the evaporation behavior of TiN coatings in atom probe tomography: a multi-instrument study, Ultramicroscopy 270 (2025) 114105, https://doi.org/10.1016/j.ultramic.2025.114105.
[28] S. Jakob, M. Thuvander, Revisiting compositional accuracy of carbides using a decreased detector efficiency in a LEAP 6000 XR atom probe instrument, Microsc. Microanal. 30 (2024), https://doi.org/10.1093/mam/ozae069.
[29] D.W. Saxey, Correlated ion analysis and the interpretation of atom probe mass spectra, Ultramicroscopy 111 (2011) 473–479, https://doi.org/10.1016/j.ultramic.2010.11.021.
[30] K. Kruska, D.K. Schreiber, Background recovery through the quantification of delayed evaporation multi-ion events in atom-probe data, Microsc. Microanal. 21 (2015) 857–858, https://doi.org/10.1017/S1431927615005085.
[31] B. Caplins, A. Chiaramonti, L. Miaja-Avila, N. Sanford, On the voltage and bowl correction of trigger-uncorrelated multihit events, Microsc. Microanal. 27 (2021) 412–415, https://doi.org/10.1017/s1431927621001999.
[32] O. Cojocaru-Mirédin, Y. Yu, J. Köttgen, T. Ghosh, C. Schön, S. Han, C. Zhou, M. Zhu, M. Wuttig, Atom probe tomography: a local probe for chemical bonds in solids, Adv. Mater. 36 (2024), https://doi.org/10.1002/adma.202403046.
[33] C. Czettl, C. Mitterer, M. Penoy, C. Michotte, M. Kathrein, C_2H_6 as precursor for low pressure chemical vapor deposition of TiCNB hard coatings, Surf. Coat. Technol. 215 (2013) 127–132, https://doi.org/10.1016/j.surfcoat.2012.08.081.
[34] C. Kainz, N. Schalk, C. Saringer, C. Czettl, In-situ investigation of the oxidation behavior of powdered TiN, Ti(C,N) and TiC coatings grown by chemical vapor deposition, Surf. Coat. Technol. 406 (2021), https://doi.org/10.1016/j.surfcoat.2020.126633.
[35] P. Ström, D. Primetzhofer, Ion beam tools for nondestructive in-situ and in-operando composition analysis and modification of materials at the Tandem Laboratory in Uppsala, JINST 17 (2022), https://doi.org/10.1088/1748-0221/17/04/P04011.
[36] M. To Baben, M. Hans, D. Primetzhofer, S. Evertz, H. Ruess, J.M. Schneider, Unprecedented thermal stability of inherently metastable titanium aluminum nitride by point defect engineering, Mater. Res. Lett. 5 (2017) 158–169, https://doi.org/10.1080/21663831.2016.1233914.
[37] B. Stelzer, X. Chen, P. Bliem, M. Hans, B. Völker, R. Sahu, C. Scheu, D. Primetzhofer, J.M. Schneider, Remote tracking of phase changes in Cr_2AlC thin films by in-situ resistivity measurements, Sci. Rep. 9 (2019) 8266, https://doi.org/10.1038/s41598-019-44692-4.
[38] M.A. Sortica, V. Paneta, B. Bruckner, S. Lohmann, M. Hans, T. Nyberg, P. Bauer, D. Primetzhofer, Electronic energy-loss mechanisms for H, He, and Ne in TiN, Phys. Rev. A (Coll Park) 96 (2017) 032703, https://doi.org/10.1103/PhysRevA.96.032703.
[39] M.V. Moro, R. Holeňák, L. Zendejas Medina, U. Jansson, D. Primetzhofer, Accurate high-resolution depth profiling of magnetron sputtered transition metal alloy films containing light species: a multi-method approach, Thin Solid Films 686 (2019), https://doi.org/10.1016/j.tsf.2019.137416.
[40] M. Tkadletz, H. Waldl, M. Schiester, A. Lechner, G. Schusser, M. Krause, N. Schalk, Efficient preparation of microtip arrays for atom probe tomography using fs-laser processing, Ultramicroscopy 246 (2023), https://doi.org/10.1016/j.ultramic.2022.113672.
[41] M.K. Miller, K.F. Russell, Atom probe specimen preparation with a dual beam SEM/FIB miller, Ultramicroscopy 107 (2007) 761–766, https://doi.org/10.1016/j.ultramic.2007.02.023.
[42] M. Hans, J.M. Schneider, Electric field strength-dependent accuracy of TiAlN thin film composition measurements by laser-assisted atom probe tomography, New J. Phys. 22 (2020), https://doi.org/10.1088/1367-2630/ab7770.
[43] F. Konstantiniuk, M. Schiester, M. Tkadletz, C. Czettl, N. Schalk, Annealing activated substrate element diffusion and its influence on the microstructure and mechanical properties of CVD TiN/TiCN coatings, Surf. Coat. Technol. (2024) 131079, https://doi.org/10.1016/j.surfcoat.2024.131079.
[44] D.R. Kingham, The post-ionization of field evaporated ions: a theoretical explanation of multiple charge states, Surf. Sci. 116 (1982) 273–301, https://doi.org/10.1016/0039-6028(82)90434-4.
[45] L. Tegg, L.T. Stephenson, J.M. Cairney, Estimation of the electric field in atom probe tomography experiments using charge state ratios, Microsc. Microanal. 30 (2024) 466–475, https://doi.org/10.1093/mam/ozae047.
[46] B. Gault, D.W. Saxey, M.W. Ashton, S.B. Sinnott, A.N. Chiaramonti, M.P. Moody, D. K. Schreiber, Behavior of molecules and molecular ions near a field emitter, New J. Phys. 18 (2016), https://doi.org/10.1088/1367-2630/18/3/033031.
[47] I. Blum, L. Rigutti, F. Vurpillot, A. Vella, A. Gaillard, B. Deconihout, Dissociation dynamics of molecular ions in high dc electric field, J. Phys. Chem. A 120 (2016) 3654–3662, https://doi.org/10.1021/acs.jpca.6b01791.
[48] E. Di Russo, I. Blum, I. Rivalta, J. Houard, G. Da Costa, F. Vurpillot, D. Blavette, L. Rigutti, Detecting dissociation dynamics of phosphorus molecular ions by atom probe tomography, J. Phys. Chem. A 124 (2020) 10977–10988, https://doi.org/10.1021/acs.jpca.0c09259.
[49] B.W. Caplins, A.N. Chiaramonti, J.M. Garcia, L. Miaja-Avila, K.H. Yano, D. K. Schreiber, J.H. Bunton, On the instrument-dependent appearance of ion dissociation events in atom probe tomography mass spectra, Ultramicroscopy 267 (2024) 114061, https://doi.org/10.1016/j.ultramic.2024.114061.
[50] T.T. Tsong, Field ion image formation, Surf. Sci. 70 (1978) 211–233, https://doi.org/10.1016/0039-6028(78)90410-7.
[51] M. Thuvander, J.J. Weidow, J. Angseryd, L.K.L. Falk, F. Liu, M. Sonestedt, K. Stiller, H.O. Andrén, Quantitative atom probe analysis of carbides, Ultramicroscopy 111 (2011) 604–608, https://doi.org/10.1016/j.ultramic.2010.12.024.
[52] J. Meija, T.B. Coplen, M. Berglund, W.A. Brand, P. De Bièvre, M. Gröning, N. E. Holden, J. Irrgeher, R.D. Loss, T. Walczyk, T. Prohaska, Isotopic compositions of the elements 2013 (IUPAC technical report), Pure Appl. Chem. 88 (2016) 293–306, https://doi.org/10.1515/pac-2015-0503.